

# Optics Letters

## Fabrication of anti-reflective micro-structure at terahertz frequency by using Chinese acupuncture needles

YUNZHOU LI,<sup>1</sup> BIN CAI,<sup>1,\*</sup> AND YIMING ZHU<sup>1</sup>

<sup>1</sup>Cooperative Innovation Centre of Terahertz Science, Engineering Research Center of Optical Instrument and System, Ministry of Education, Shanghai Key Lab of Modern Optical System, University of Shanghai for Science and Technology, Shanghai 200093, China

\*Corresponding author: bullcai@gmail.com

Received 27 April 2015; revised 22 May 2015; accepted 26 May 2015; posted 26 May 2015 (Doc. ID 239826); published 15 June 2015

**A terahertz (THz) anti-reflective structure on a polystyrene layer was fabricated by using a handmade metallic mold comprising a bunch of Chinese acupuncture needles. Polystyrene was spin-coated onto a silicon substrate and then deformed by the mold via a hot-embossing process. The deformed layer yielded gradient refractive index profiles on the substrate. Compared with a common single antireflective layer, we observed an increase of ~20% in the transmittance. We also observed broader bandwidth properties compared with the single layer structure. The process imposes no substrate limiting, i.e., it can be applied onto various THz device surfaces for antireflection purpose.** © 2015 Optical Society of America

**OCIS codes:** (040.2235) Far infrared or terahertz; (310.1210) Antireflection coatings; (220.4000) Microstructure fabrication.

<http://dx.doi.org/10.1364/OL.40.002917>

A THz wave is a kind of electromagnetic wave, typically within the frequency range of 0.1–10 THz (1 THz =  $10^{12}$  Hz), between microwave and infrared radiation regions [1]. THz waves share benefits of both microwaves and infrared radiations [2]. Like microwaves, they can easily penetrate nonconductive materials, such as clothing and plastics; meanwhile, they can carry a large amount of information, similarly to infrared radiation [3]. The THz wave therefore exhibits considerable potential for applications, such as safety inspection, organic compounds characterization, etc. However, the energy levels as well as conversion efficiencies of the THz waves generated by compact THz sources, e.g., photoconductive antennas, are relatively low, which suppress the development of THz systems [4]. Thus, it is important to maintain the THz wave energy during the wave propagation and processing. THz components usually suffer surface reflection loss (for example, approximately 50% energy will be reflected away from a bare silicon substrate) and Fabry–Perot resonance [5,6]; therefore, antireflection is a very important issue for many THz devices.

Coating a quarter-wave thickness with low-refractive-index dielectric material onto the surface of THz devices is one of the traditional antireflective techniques [7]. Owing to the canceling interference between the first- and second-order reflected waves, an antireflective effect can be realized. Although this method can yield a low reflection, however, the narrowband property and the difficulty of finding coating materials with suitable refractive index make it unsuitable for broadband applications. The sub-wavelength surface relief structure array is another advanced approach to realize antireflective properties [8–10]. The surface relief structure yields a gradient refractive index profile that can not only minimize the Fresnel reflection loss but also leads to a broadband and omnidirectional antireflective effect. In order to realize this kind of antireflective effect, many surface relief structures were proposed, including micro-pyramids [11] and micro-hemisphere arrays [12]. Those two structures above yielded a minimum reflectance of 3%, and 1.8% in broad THz ranges, respectively. Although those structures obtain excellent antireflective effects, they suffer disadvantages, such as complicated fabrication, long processing time, potential risk of using toxic chemical reagents (e.g., in etching process), and especially substrate limitation (e.g., etching micro-pyramid antireflective structure is a special case of crystalline silicon substrate). A polymer is a versatile material that has an excellent processability. It is also light, low-cost, and highly transparent in the THz region for some nonpolarized species [13]. Furthermore, polymer can hybridize with nanoparticles. This offers a great potential of refractive index tuning, which is a very important advantage when a refractive index matching is required [14]. By utilizing the thermal deformation property of polymers, many microstructure formation techniques such as nano-imprinting [15] and micro-contact printing [16], hot-embossing [17,18] techniques have been developed to fabricate nano and microstructure patterns easily. In this study, in order to fabricate a sub-wavelength surface relief structure pattern, a metallic mold that comprises a bunch of Chinese acupuncture needles was used to deform a cast polymer layer by a hot-embossing technique. By this simple process, a gradient effective refractive index profile for the antireflection was constructed successfully on a silicon

wafer's surface. The transmittances of the samples in the THz range were investigated with a THz-time domain spectroscopy (THz-TDS) system. The microstructure was highly efficient, which could significantly decrease the surface reflection of the substrate. This process is versatile and can be easily applied to various THz devices, such as THz sources, receivers, and filters, etc.

High-resistant (HR) silicon is highly transparent in the THz range [19,20]; therefore, it is often used to fabricate THz components such as THz lenses and filters. However, owing to the high refractive index of silicon, silicon devices always suffer a high surface reflection loss (approximately 50%). In this study, to demonstrate the performances of the embossed antireflective structures, 500- $\mu\text{m}$ -thick double-side-polished HR silicon wafers were used as the antireflective layers' substrates and as the comparative targets.

We chose a highly transparent polymer polystyrene (PS, refractive index  $n \approx 1.59$ ) as the deformation material to apply the hot embossing process. Compared with other popular THz polymers, e.g., polyethylene (PE,  $n \approx 1.51$ ), polymethylpentene (TPX,  $n \approx 1.46$ ), and cyclo olefin polymer (COP,  $n \approx 1.52$ ), the PS exhibits not only good solubility and transparency but also a comparatively high refractive index in the THz region [21], which is particularly advantageous for matching the refractive index with the silicon substrate. The PS powder was dissolved into a toluene solvent, and then filtering and concentrating processes were applied to the solution, followed by spin coating onto the silicon substrate.

The whole process includes three simple steps. First, a to-be-deformed polymer layer was spin-coated on a HR silicon substrate. Then, the substrate and handmade metallic mold was heated to the glass transition temperature of PS (approximately 110°C), and the mold was pressed to deform the polymer layer (the pressure was approximate 50 N) in an air environment. Finally, after the system was cooled to room temperature, the metallic mold was demolded. In order to compare the antireflective performance with that of a monolayer, the coating thickness was regulated to the quarter-wavelength. For example, when the THz wave has a center frequency of 0.4 THz (wavelength  $\lambda \approx 750 \mu\text{m}$ ), the corresponding thickness of the coating is approximately 120  $\mu\text{m}$  (thickness =  $\lambda/4n$ , where  $n$  is the refractive index of the coating material).

An illustration of the metallic mold used for the hot embossing is presented in Fig. 1(a). This handmade metallic mold comprised a set of tightly bundled Chinese acupuncture needles attached together by a coil heater. A scanning electron microscope (SEM) image of a needle tip is shown in Fig. 1(b). The needle has a diameter in the range of  $120 \pm 20 \mu\text{m}$ , the length of tip is 300–400  $\mu\text{m}$  with a cone angle of 23°–24°, and the dimension is lower than the targeted THz wavelength (3 mm–200  $\mu\text{m}$ ).

By the hot-embossing process, the flat PS layer was deformed into holes and annular bulges that were originated by the extrusion of the needle tips [Fig. 2(a)]. The internal shape of the holes was intended as a cone reversed against the needle tip as indicated by the inset of the Fig. 2(a), where hole diameters ( $D = 2R$ ) are in the range of 30–60  $\mu\text{m}$ , and annulus widths ( $d = 2r$ , difference between the inner and outer diameters) are in the range of 20–40  $\mu\text{m}$ . The micro-structured PS layer can be considered as a series of thin layers with continuously

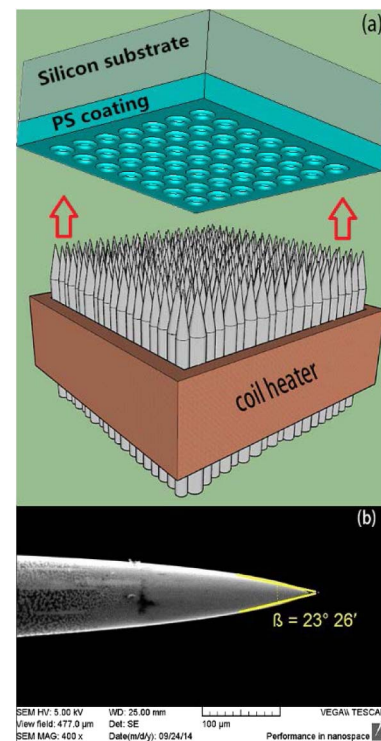


**Fig. 1.** (a) Illustration of handmade metallic mold. (b) SEM image of Chinese acupuncture needle tip.

changing filling factors. The effective refractive index ( $n_{\text{eff}}$ ) of each layer can be expressed by Eq. (1), where  $n_{\text{air}}$  is the refractive index of air,  $S_{\text{air}}\%$  is the fraction of the air area,  $n_{\text{ps}}$  is the refractive index of PS, and  $S_{\text{ps}}\% (= 1 - S_{\text{air}}\%)$  is the fraction of the PS area:

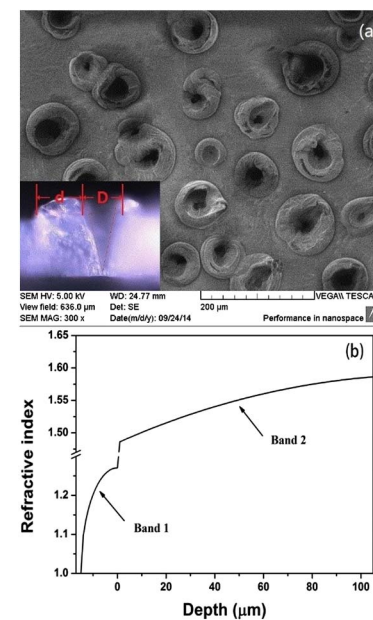


**Fig. 2.** (a) SEM image of antireflection structure obtained by hot embossing. (b) Effective refractive index profile of fabricated surface relief structure, calculated with Eq. (1).

$$n_{\text{eff}} = (n_{\text{air}}^2 \times S_{\text{air}}\% + n_{\text{PS}}^2 \times S_{\text{PS}}\%)^{1/2}. \quad (1)$$

The refractive index profile of the micro-structured PS layer can be roughly calculated with Eq. (1), and the result is shown in Fig. 2(b). We obtained two gradually changing index profiles. Band 1, from 1.00 to 1.28 (−15–0 μm), is ascribed to the annular bulges, and Band 2, from 1.49 to 1.59 (0–120 μm), is ascribed to the reversed cone structure. In Fig. 2(b), the minus values on the abscissa refer to the height above the plane of the PS layer, and the plus values refer to the depth from the plane, the zero is at the interface between air and the PS layer. For a perfect antireflective structure, a gradient index profile in the range of 1.00–3.42 is necessary. This necessitates the further study of structure tuning and coating-material preparation.

A THz-TDS system (FiCO, at Zomega Corp.) was used to evaluate the transmittances of the samples with a valid bandwidth from 0.1–1.5 THz. The deformed PS layer not only can bring an antireflective effect but also probably causes an extra scattering loss of the incident THz radiation. The scattered radiation is difficult to be directly detected; therefore, instead of the reflectance, we measured the transmittance of the samples. To minimize the disturbance of the Fabry–Perot effect, only the primary pulse in time domain was used. The experiment results are shown in Fig. 3, where the *y*-axis represents the transmitted intensity, and the *x*-axis represents the frequency of the THz radiation. In Fig. 3, the black solid line is the transmitted intensity of a bare HR silicon substrate; because of the large surface reflection, only 50% transmittance can be achieved. When a 120-μm PS antireflection layer was coated on the substrate, two enhanced peaks appeared (red dashed-dotted line in Fig. 3) at 0.37 THz (811 μm) and 1.10 THz (270 μm). These two peaks correspond to the canceling interferences between the first- and second-order reflections of 0.37 and 1.10 THz after phase shifts of  $\pi$  and  $3\pi$ , respectively.

To verify the experimental data, we simulated the transmittances of the samples by the CST MICROWAVE STUDIO. For the embossed samples, the structure shown in Fig. 2(a) was used ( $D = 60$ ,  $d = 30$ ), and the simulation model and results are shown in Figs. 4(a) and 4(b). In the simulation, the THz radiation was irradiated normally to the samples, and absorption loss as well as refractive index dispersion of the PS material were not considered.

The pink dotted line in Fig. 4(b) indicates the transmittance of the single-side embossed PS/silicon sample. From the simulation, we can see that with the relief structure, the sample

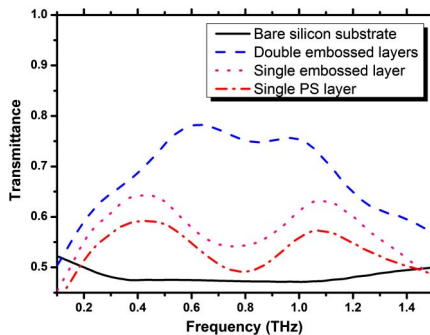


**Fig. 3.** Experimental result of the transmittance spectra of the bare HR-Si, single-layer PS, single hot-embossed PS layer, and double-side PS with hot-embossed samples.

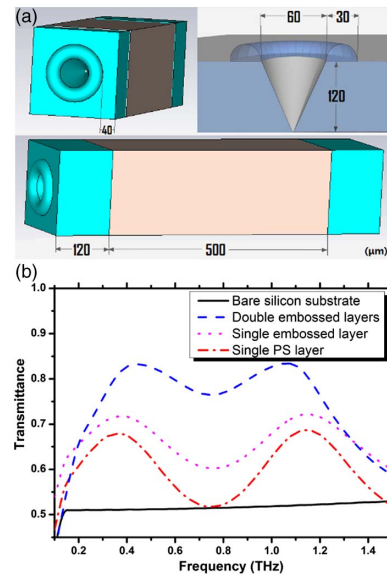


**Fig. 4.** (a) Simulation model, the diameter of the cone ( $D = 60$  μm), the diameter of the annular bulge ( $d = 30$  μm), the space between each unit ( $\sim 40$  μm), the thickness of the PS layer ( $H_{\text{ps}} = 120$  μm), and the thickness of the silicon substrate ( $H_{\text{s}} = 500$  μm) were marked. (b) Simulation result of the transmittance spectra of the bare HR-Si, single-layer PS, single hot-embossed PS layer, and double-side PS with hot-embossed samples.

exhibited an increased transmittance throughout the frequency range of 0.1–1.5 THz. Meanwhile, the interference between the first and second reflections of the coated layer became weaker than the nonprocessed one [red dashed-dotted line in Fig. 4(b)]. The simulation agrees well with the experiment results. For the double-side embossed sample, the transmittance can be further enhanced, and the highest transmittance was achieved [blue dashed line in Fig. 4(b)]. In the experiment, we obtained an approximately 20% enhancement than that of the single layer coated HR silicon substrate. The experimental peaks slightly deviate from the theoretical simulation peaks; this may be because the incident THz waves were not perfectly normal to the sample’s surface and the thickness of the PS layer were not precisely controlled. In addition, the simulated data exhibit values 4%–7% higher than those of the experimental data; this could be due to the absorption of the silicon and PS layer. Here, it must be noted that because of the refractive index gap ( $\Delta n = 1.83$ ) between the PS and silicon substrate, the reflectance at the PS/silicon interface is inevitable due to the refractive index mismatching. Thus, achieving a high refractive index and highly transparent THz materials is the foremost challenge.

The measured transmittance spectra of the bare silicon substrate, single-layer PS coated, and double-sided embossed samples with Fabry–Perot resonance effects are plotted in Fig. 5. The free spectral range (FSR) of the bare silicon substrate is approximately 0.09 THz because of the multi-reflection inside the 500-μm-thick silicon substrate. As the antireflective effect increased, the Fabry–Perot resonances decreased significantly. The interference intensities near 0.4 THz (ratio of transmittance peak to valley) were 3.33, 1.64, and 1.23 for the bare silicon substrate, single PS layer sample, and double-side

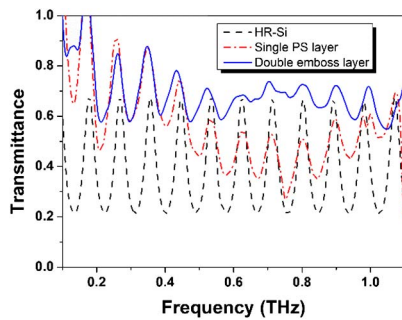


**Fig. 5.** Transmittance spectra of the samples, with Fabry–Perot resonance effect.

embossed sample, respectively. This is beneficial for improving the THz beam quality and thereby increasing the signal-to-noise ratio of THz systems.

In conclusion, Chinese acupuncture needles were utilized for a metallic mold, and hot embossing was applied to form a gradient refractive index profile for antireflection in the THz region. Using this very-low-cost equipment and simple process, we increased the transmittance from 50%, for a bare silicon substrate, to approximately 75%, which is  $\sim 20\%$  higher than that of single antireflective layer. The proposed structure provides a far broader bandwidth (0.1–1.5 THz) than the single-layer antireflective structure and can decrease the Fabry–Perot resonance effectively. In contrast with other surface relief structure fabrication methods, hot embossing imposes less substrate limiting and can therefore be applied onto various THz substrates and devices. By optimizing the mold structure, coating material, and other design parameters, the antireflective effect can be further enhanced.

Key Scientific and Technological Project of Science and Technology Commission of Shanghai Municipality (STCSM) (12142200100, 12JC1407100); Major National Development Project of Scientific Instrument and Equipment (2011YQ150021, 2012YQ14000504); National Natural Science Foundation of China (NSFC) (1377111, 61138001, 61205094, 61307126); National Program of Key Basic Research Project of China (973 Program) (2014CB339806); Program for New Century Excellent Talents in University (New Century Excellent Talents

Program) (NCET-12-1052); Program of Shanghai Subject Chief Scientist (14XD1403000); Scientific Research Innovation Project of Science and Technology Commission of Shanghai Municipality (STCSM) (12510502300).

## REFERENCES

1. B. Ferguson and X. C. Zhang, *Nat. Mater.* **1**, 26 (2002).
2. J. Xu, L. Chen, L. Xie, S. Du, M. Yuan, Y. Peng, and Y. Zhu, *Plasmonics* **8**, 1293 (2013).
3. M. Tonouchi, *Nat. Photonics* **1**, 97 (2007).
4. X. Hu, Y. Li, F. Fang, X. Li, J. Li, Y. Chen, X. Zhang, L. Chai, C. Wang, A. B. Fedotov, and A. M. Zheltikov, *Opt. Lett.* **38**, 2053 (2013).
5. C. H. Sun, P. Jiang, and B. Jiang, *Appl. Phys. Lett.* **92**, 061112 (2008).
6. C. Brückner, T. Käsebier, B. Pradarutti, S. Riehemann, G. Notni, E. B. Kley, and A. Tünnermann, *Opt. Express* **17**, 3063 (2009).
7. H. Chen, J. Zhou, J. F. O'Hara, F. Chen, A. K. Azad, and A. J. Taylor, *Phys. Rev. Lett.* **105**, 073901 (2010).
8. C. Brückner, B. Pradarutti, O. Stenzel, R. Steinkopf, S. Riehemann, G. Notni, and A. Tünnermann, *Opt. Express* **15**, 779 (2007).
9. A. Thoman, A. Kern, H. Helm, and M. Walther, *Phys. Rev. B* **77**, 195405 (2008).
10. R. Datta, C. D. Munson, M. D. Niemack, J. J. McMahon, J. Britton, E. J. Wollack, J. Beall, M. J. Devlin, J. Fowler, P. Gallardo, J. Hubmayr, K. Irwin, L. Newburgh, J. P. Nibarger, L. Page, M. A. Quijada, B. L. Schmitt, S. T. Staggs, R. Thornton, and L. Zhang, *Appl. Opt.* **52**, 8747 (2013).
11. Y. W. Chen, P. Y. Han, and X. C. Zhang, *Appl. Phys. Lett.* **94**, 041106 (2009).
12. D. S. Kim, D. J. Kim, D. H. Kim, S. Hwang, and J. H. Jang, *Opt. Lett.* **37**, 2742 (2012).
13. C. S. Ponseca, Jr., R. Pobre, E. Estacio, N. Sarukura, A. Argyros, M. C. J. Large, and M. A. Van Eijkelenborg, *Opt. Lett.* **33**, 902 (2008).
14. B. Cai, O. Sugihara, H. I. Elim, T. Adschiri, and T. Kaino, *Appl. Phys. Express* **4**, 092601 (2011).
15. A. Pierret, M. Hocevar, S. L. Diedenhofen, R. E. Algra, E. Vlieg, E. C. Timmering, M. A. Verschuuren, G. W. G. Immink, M. A. Verheijen, and E. P. A. M. Bakkers, *Nanotechnology* **21**, 065305 (2010).
16. S. H. Hong, J. Hwang, and H. Lee, *Nanotechnology* **20**, 385303 (2009).
17. C. J. Ting, M. C. Huang, H. Y. Tsai, C. P. Chou, and C. C. Fu, *Nanotechnology* **19**, 205301 (2008).
18. K. S. Han, H. Lee, D. Kim, and H. Lee, *Sol. Energy Mater. Sol. Cells* **93**, 1214 (2009).
19. E. V. Pechen, S. Vent, B. Brunner, A. Prückl, S. Lipp, G. Lindner, O. Alexandrov, J. Schützmann, and K. F. Renk, *Appl. Phys. Lett.* **61**, 1980 (1992).
20. A. Brahm, S. Döring, A. Wilms, G. Notni, S. Nolte, and A. Tünnermann, *Appl. Opt.* **53**, 2886 (2014).
21. B. Bowden, J. A. Harrington, and O. Mitrofanov, *Opt. Lett.* **32**, 2945 (2007).